Quantitative analysis of the complex magnetic phase diagram of HoAlGa

A. R. Ball, D. Gignoux, D. Schmitt, and F. Y. Zhang
Laboratoire Louis Néel, CNRS, 166X, 38042 Grenoble CEDEX 9, France
(Received 20 July 1992; revised manuscript received 7 December 1992)

A recent self-consistent periodic-field model, set up for long-period magnetic systems, is shown to give a satisfactory quantitative description of the main features of a complex magnetic phase diagram below T_N of an antiferromagnet, namely the hexagonal HoAlGa compound. From the crystal-field and exchange parameters it has been possible to account for (i) the multistep magnetization processes with the correct values of the transition field and the intermediate structures along the easy axis, (ii) magnetization curves along the hard axes, (iii) the amplitude and direction of each moment during all these processes, (iv) the reduced value of the specific-heat discontinuity of the λ anomaly at T_N.

I. INTRODUCTION

Rare-earth-based uniaxial intermetallic systems are particularly exciting because (i) uniaxial anisotropy gives rise to either Ising-like or X-Y-like properties, (ii) competing exchange interactions, due to their long-range and oscillatory character, give rise to a maximum of the Fourier transform $J(\mathbf{q})$ for a $\mathbf{q}$ value which has no reason to be commensurate with the crystallographic reciprocal lattice. In particular, incommensurate sine wave modulated magnetic structures are frequently stabilized just below the Néel temperature. In a large number of antiferromagnetic compounds, such structures transform at low-temperature to equal moment ones. One then observes complex field-temperature magnetic phase diagrams, characterized by additional transitions below T_N and multistep metamagnetic processes at low temperature. Nowadays special attention is paid, experimentally as well as theoretically, to the microscopic and macroscopic aspects of such magnetic phase diagrams observed in an increasing number of compounds.[1–3]

In this context, the $R\mathrm{Ga}_2$ and $R(\mathrm{Al}_x\mathrm{Ga}_{1-x})_2$ compounds present a large variety of frustrated magnetic arrangements in a very simple hexagonal structure.[4] In particular, they give an excellent example of the different magnetic arrangements which can be stabilized in a two-dimensional triangular lattice in both Ising-like and X-Y-like systems. These compounds crystallize in the AlB_2-type hexagonal structure (space group $P6/mmm$), the rare-earth atom lying in the $1a$ (0,0,0) position whereas Al or Ga lies randomly in the $2e$ $(\frac{1}{3},\frac{2}{3},\frac{1}{2})$ and $(\frac{2}{3},\frac{1}{3},\frac{1}{2})$ positions. Al and Ga atoms are not magnetic.

This paper is devoted to the HoAlGa compound which offers the opportunity to apply a recent model to the quantitative approach of a complex magnetic phase diagram. This self-consistent periodic-field (PF) model, based on the mean-field approximation in a long-period magnetic structure, was successfully used to the quantitative description of (i) the strong reduction of the specific-heat discontinuity at T_N in compounds (with and without magnetocrystalline anisotropy) having sine wave modulated magnetic structures below T_N,[5,6] (ii) the metamagnetic process of this type of structure in the $\mathrm{PrNi}_2\mathrm{Si}_2$ compound in which the modulation is stable down to 0 K on account of a crystal-field singlet ground state.[7] Here we show that this model can be successfully applied to a compound such as HoAlGa exhibiting a complex magnetic phase diagram characterized in particular by sine wave modulation just below T_N and multistep metamagnetic processes associated with equal moment configurations at low temperature. Indeed from the knowledge of (i) crystalline-electric-field (CEF) parameters determined in the paramagnetic domain, (ii) the paramagnetic exchange parameters $J(\mathbf{Q})$ and $J(0)$, and (iii) the magnetic periodicity at T_N, this model gives a remarkable quantitative description of the magnetic and thermodynamic properties of this compound below T_N.

Previous studies in this compound[8,9] using several techniques such as magnetization measurements, specific heat, neutron diffraction on a polycrystal without field and on a single crystal under an applied field have shown the following characteristics. At low temperature (phase I), HoAlGa presents an equal moment (EM) magnetic structure characterized by the commensurate propagation vector $\mathbf{Q}_1=(\frac{1}{3},\frac{1}{3},\frac{1}{2})$ and its harmonic of third order $3\mathbf{Q}_1=(0,0,\frac{1}{2})$, the Ho moments lying along the [001] crystallographic direction (Fig. 1). A transition was observed at $T_t=18.5$ K by neutron diffraction on polycrystal. Between this temperature and $T_N=31$ K (phase II), HoAlGa has a sine wave modulated structure with an incommensurate propagation vector $\mathbf{Q}_2=(\frac{1}{3},\frac{1}{3},0.481)$. Along the easy [001] direction magnetization processes depend on temperature. In the latter temperature range, magnetization curves exhibit a smooth transition toward the ferromagnetic state. Between 18.5 and 6 K, a two-step metamagnetic process is observed, the intermediate-field-induced phase having the $\mathbf{Q}_2$ propagation vector. Below 6 K, the metamagnetic process is still sharper and has three steps. The second field-induced phase is still associated with $\mathbf{Q}_2$ whereas the first field-induced phase (phase III) occupies a small area of the H-T phase diagram and is characterized by the same components $(\frac{1}{3},\frac{1}{3})$ of the propagation vector in the basal plane and a periodicity along $\mathbf{c}$ six times larger than the crystallographic one. These studies have shown that HoAlGa exhibits a complex H-T phase diagram along the [001] easy axis.

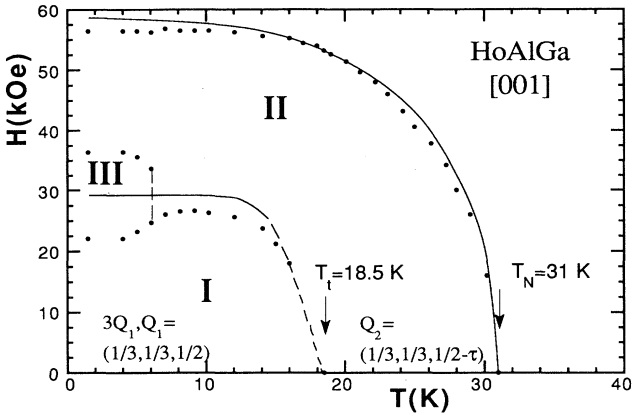

FIG. 1. Experimental and calculated boundaries of the phase diagram of HoAlGa along the easy [001] axis.

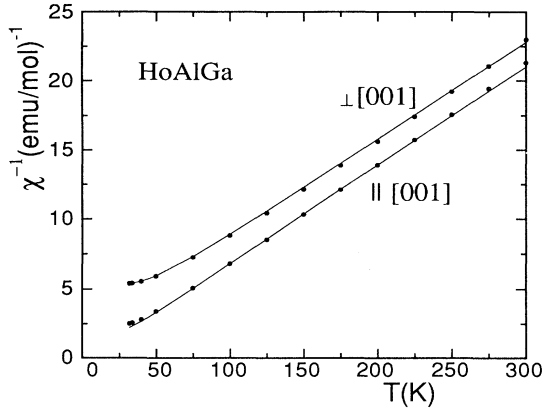

FIG. 3. Temperature dependence of the reciprocal susceptibility in HoAlGa along and perpendicular to the easy [001] magnetization direction. Lines are calculated variations.

As the knowledge of CEF and exchange coefficients is required to use the PF model, the first part of this paper is devoted to their determination in the paramagnetic range from neutron spectroscopy on a polycrystal and field dependences of magnetization and thermal dependence of susceptibility on a single crystal (Secs. II and III). The formalism and its application to the description of the magnetic phase diagram and thermal properties such as susceptibility and specific heat below T_N are presented in the second part (Sec. IV).

II. EXPERIMENTAL RESULTS

A. Bulk paramagnetic properties

Magnetization measurements have been performed along the three main symmetry directions of the hexagonal unit cell, on a single crystal grown using the Bridgman technique. Magnetization was measured using the extraction method in magnetic fields up to 8 T and in the temperature range 1.5–300 K. In the paramagnetic state, i.e., above 31 K, the magnetization is anisotropic, the [001] direction being noticeably easier than the basal plane (Fig. 2). Within the latter, a very small anisotropy can be detected, the magnetization being slightly larger (about 1%) along the [120] direction.

The thermal dependence of the paramagnetic reciprocal susceptibility along and perpendicular to [001] is reported in Fig. 3. Above 100 K, a Curie-Weiss behavior is observed with the same effective moment of $10.5\mu_B$ along both directions, in close agreement with the free Ho^{3+}-ion value. Paramagnetic Curie temperatures are -20 and 9 K perpendicular and parallel to **c**, respectively. From their difference, a first estimation of the second-order CEF parameter can be made, i.e., $B_2^0 = -0.28$ K. Below 100 K where higher-order CEF terms play an increasing role, deviations from the linear variations occur. Because of the number of parameters these deviations are not very selective for the determination of the CEF parameters. However, analyzing these thermal dependences of the paramagnetic susceptibility remains fundamental and complementary to other experiments.

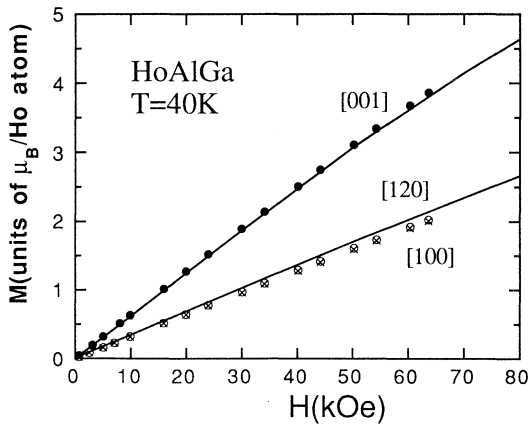

FIG. 2. Field dependence of the magnetization of HoAlGa along the [001] (solid circles), [100] (crosses), and [120] (open circles) directions at 40 K; lines are calculated variations.

B. Neutron spectroscopy

We diluted holmium in yttrium in order to lower the magnetic interactions and study the compound in the paramagnetic state at a temperature where only the ground level is populated. The compounds studied were $Ho_{0.25}Y_{0.75}AlGa$ ($T_N = 4.5$ K) and YGa_2. The latter was studied for the correction of the phonon contribution to the spectra. Polycrystalline samples were prepared by high-frequency melting of the stoichiometric amounts of constituents under an argon atmosphere.

The inelastic-neutron-scattering experiments were performed on the IN4 time-of-flight spectrometer at the ILL (Grenoble) with neutrons of incident energy $E_0 = 17.2$ meV and $E_1 = 68.9$ meV at various temperatures ranging from 10 to 130 K, within the paramagnetic phase of

$Ho_{0.25}Y_{0.75}AlGa$. Spectra were collected for scattering angles 2θ ranging between 4° and 140°, in order to follow the **Q** dependence of the magnetic as well as phonon scattering. All the measured spectra were first corrected for the background signal, yielding the total normalized response referenced to a vanadium standard.[10] A second correction was then performed, namely, subtracting the phonon contribution obtained on the nonmagnetic polycrystalline compound YGa_2. For this compound, large phonon scattering is clearly observed at 10, 17, and 35 meV.[11] Using a scaling procedure that takes into account the Q dependence of this contribution as explained in Ref. 10, we could extrapolate the phonon contribution in $Ho_{0.25}Y_{0.75}AlGa$. Subtracting this from the total spectra finally provided the magnetic spectral response in $Ho_{0.25}Y_{0.75}AlGa$, shown in Fig. 4 for the low incident energy E_0.

At low temperature but above T_N, three well-defined inelastic transitions are observed at about $\Delta_1=3.52$ meV, $\Delta_2=6.65$ MeV, and $\Delta_3=11.56$ meV. From their temperature and **Q** dependence, the two highest-energy transitions can be attributed to CEF excitations from the ground state to excited levels. The low-energy transition increases in intensity strongly when temperature increases from 10 to 40 K, in contrast with the two others. Therefore, at least to a large extent, it corresponds to a transfer between two excited levels. Using a higher neutron incident energy we did not observe any additional magnetic transition up to 40 meV.

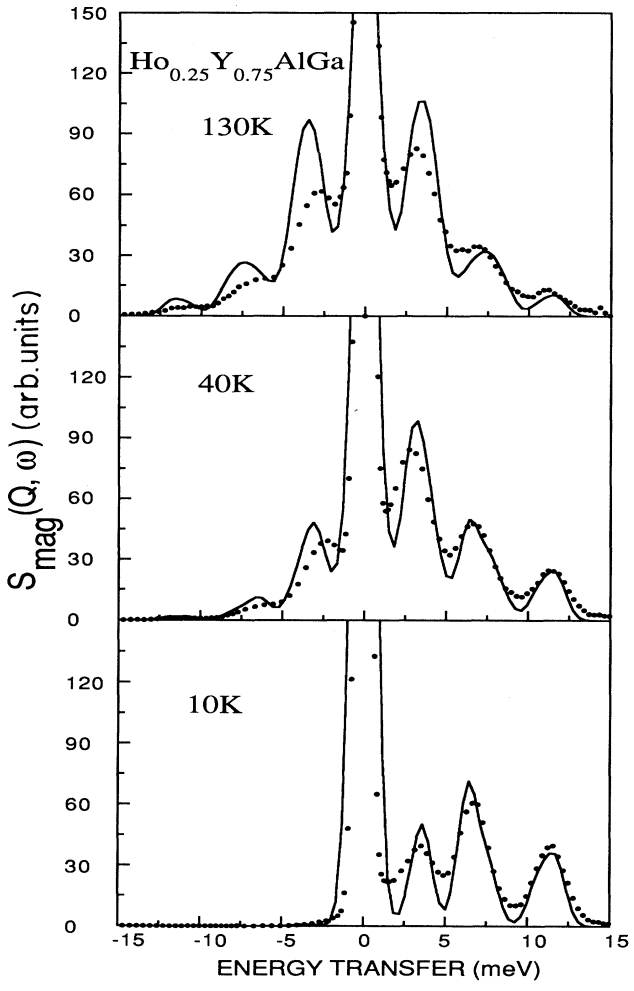

FIG. 4. Magnetic spectral response of $Ho_{0.25}Al_{0.75}Ga$ at 10, 40, and 130 K for an incident neutron energy of 17.2 meV and a scattering angle of 20°. Lines are calculated variations.

III. CRYSTAL-FIELD DETERMINATION

A. Formalism

The Hamiltonian used for describing the magnetic properties of a $4f$ shell in the paramagnetic phase is written as

$$\mathcal{H}=\mathcal{H}_{\mathrm{CEF}}+\mathcal{H}_Z+\mathcal{H}_B \ . \tag{1}$$

Using the operator equivalent method and the z axis being parallel to the [001] direction, the CEF term $\mathcal{H}_{\mathrm{CEF}}$ in the hexagonal symmetry can be written as

$$\mathcal{H}_{\mathrm{CEF}}=B_2^0O_2^0+B_4^0O_4^0+B_6^0O_6^0+B_6^6O_6^6 \ , \tag{2}$$

where the O_l^m's and B_l^m's are the Stevens equivalent operators and CEF parameters, respectively:[12]

$$\mathcal{H}_Z=g_J\mu_B\mathbf{H}\cdot\mathbf{J} \tag{3}$$

represents the Zeeman coupling between the $4f$ magnetic moment and the internal magnetic field **H** (external field corrected for demagnetization effects),

$$\mathcal{H}_B=g_J\mu_B\mathbf{H}_{\mathrm{ex}}\cdot\mathbf{J} \tag{4}$$

is the isotropic Heisenberg-type bilinear interaction Hamiltonian written in the mean-field approximation as a function of the paramagnetic exchange field $\mathbf{H}_{\mathrm{ex}}$ acting on a given ion:

$$\mathbf{H}_{\mathrm{ex}}=n\mathbf{M}=-ng_J\mu_B\langle\mathbf{J}\rangle \ , \tag{5}$$

where

$$n=\frac{1}{(g_J\mu_B)^2}J(0)=\frac{1}{(g_J\mu_B)^2}\frac{3\theta^*k_B}{J(J+1)} \ . \tag{6}$$

n or θ^* is the isotropic paramagnetic bilinear exchange parameter proportional to the Fourier transform $J(\mathbf{q})$ of the exchange interactions at $\mathbf{q}=0$. Here anisotropic bilinear couplings are neglected as well as higher-order couplings such as magnetoelastic or two-ion quadrupolar interactions.[13]

Without any external or exchange magnetic field, the diagonalization of the isolated CEF Hamiltonian $\mathcal{H}_{\mathrm{CEF}}$ provides the CEF eigenvalues and eigenstates, according to the raising of degeneracy of the $4f$ ground multiplet. For the Ho^{3+} ion ($J=8$) the $\mathcal{D}_8$ representation of the rotation group can be reduced to

$$\mathcal{D}_8=2\Gamma_1+\Gamma_2+\Gamma_3+\Gamma_4+3\Gamma_5+3\Gamma_6 \ , \tag{7}$$

where Γ_i's are the irreducible representations of the hexagonal point group D_{6h}.[14] In the $|J,M_J\rangle$ basis for the $4f$

TABLE I. Different CEF states Γ_i, associated energies E_i, and eigenfunctions Ψ_i for the Ho^{3+} ion ($J=8$) in HoAlGa; also are indicated the corresponding states Γ_i for which transitions Γ_i-Γ_j are allowed.

Label Γ_i	E_i (K)	Eigenfunction $\Psi_i=\sum_j \alpha_{ij}\|j\rangle$	Allowed transitions
$\Gamma_5^{(1)}$	136.74	$0.92\|\pm8\rangle+0.37\|\pm2\rangle-0.12\|\mp4\rangle$	$\Gamma_3,\Gamma_4,\Gamma_6^{(1)},\Gamma_6^{(2)},\Gamma_6^{(3)}$
$\Gamma_5^{(3)}$	123.99	$-0.89\|\pm2\rangle+0.39\|\pm8\rangle+0.24\|\mp4\rangle$	$\Gamma_3,\Gamma_4,\Gamma_6^{(1)},\Gamma_6^{(2)},\Gamma_6^{(3)}$
$\Gamma_1^{(1)}$	88.83	$0.59(\|6\rangle+\|-6\rangle)+0.56\|0\rangle$	$\Gamma_6^{(1)},\Gamma_6^{(2)},\Gamma_6^{(3)}$
$\Gamma_6^{(3)}$	75.42	$-0.97\|\pm1\rangle+0.21\|\mp5\rangle-0.13\|\pm7\rangle$	$\Gamma_1^{(1)},\Gamma_1^{(2)},\Gamma_2,\Gamma_5^{(1)},\Gamma_5^{(2)},\Gamma_5^{(3)}$
Γ_2	74.16	$\frac{\sqrt{2}}{2}(\|-6\rangle-\|6\rangle)$	$\Gamma_6^{(1)},\Gamma_6^{(2)},\Gamma_6^{(3)}$
$\Gamma_1^{(2)}$	42.03	$-0.83\|0\rangle+0.40(\|6\rangle+\|-6\rangle)$	$\Gamma_6^{(1)},\Gamma_6^{(2)},\Gamma_6^{(3)}$
$\Gamma_6^{(1)}$	0	$\pm0.99\|\pm7\rangle\mp0.13\|\pm1\rangle\pm0.02\|\mp5\rangle$	$\Gamma_1^{(1)},\Gamma_1^{(2)},\Gamma_2,\Gamma_5^{(1)},\Gamma_5^{(2)},\Gamma_5^{(3)}$

CEF states, the associated eigenfunctions are given in Table I. Note that the mixing coefficients α_{ij} (see Table I) in the Γ_1, Γ_5, and Γ_6 states are related to the off-diagonal terms in the CEF Hamiltonian, namely, the B_6^6 parameter. Moreover, this mixing results in an anisotropy of the magnetization within the basal plane between the [100] and [120] directions. The weak experimental anisotropy observed in HoAlGa then provides an upper limit for the B_6^6 parameter. The selection rules for the possible transitions between CEF states are also given in Table I.

B. Determination of CEF parameters

The CEF parameters and paramagnetic bilinear exchange parameter n, i.e., $J(0)$, are determined from an analysis of both of the above experiments, namely, inelastic scattering on a polycrystal, paramagnetic susceptibility, and magnetization measurements on a single crystal. Indeed each of these experiments gives information not accessible from the other.

From the anisotropy of the paramagnetic susceptibility between the basal plane and the sixfold direction [001], the sign and the amplitude of the second-order CEF parameter was, in a first stage, fixed at $B_2^0=-0.28$ K. From the small anisotropy of magnetization in the basal plane (the [120] axis is a little easier than the [100] axis) we have determined that B_6^6 is positive. Within these assumptions we carried out a grid check of the parameters B_4^0 and B_6^0, using each possible couple of values with different fixed values of B_6^6 to refine the paramagnetic susceptibility. This way we found three possible groups of parameters which fit satisfactorily the experimental data. The calculated variations are the same for the three groups (solid lines of Fig. 3). Apart from B_2^0, from one group to the other the CEF parameters are quite different in order of magnitude as well as in sign. Among these parameter groups, only one accounts for the inelastic-scattering spectra (Fig. 4) and the magnetization measurements just above the ordering temperature T_N (Fig. 2), whereas large discrepancies arise for the two other groups. Therefore, this joint analysis led us to the determination of the four CEF parameters of HoAlGa, i.e., $B_2^0=-0.27$ K, $B_4^0=-6.8\times10^{-4}$ K, $B_6^0=4.3\times10^{-5}$ K, and $B_6^6=1.5\times10^{-4}$ K (uncertainties are less than 5%) (Table II). The corresponding overall CEF splitting of the $^5I_8$ multiplet of the Ho^{3+} ion is reported in Fig. 5 together with the main transitions observed at 10 K and at higher temperatures on the neutron spectra. The width of the arrows is proportional to the probability of the transitions between the levels concerned. The $J(0)$ parameter determined from susceptibility and magnetization measurements is -0.47 K.

The three energy transfers observed at 10 K correspond to transitions from the $\Gamma_6^{(1)}$ ground state. Δ(I) involves the $\Gamma_1^{(2)}$ first excited state. Δ(II) involves mainly the Γ_2 and $\Gamma_6^{(3)}$ states and a weak contribution of $\Gamma_1^{(1)}$. Finally Δ(III) concerns the $\Gamma_5^{(3)}$ and $\Gamma_5^{(1)}$ states. The large intensity increase of Δ(I) originates from the thermal population of the $\Gamma_1^{(2)}$ first excited state allowing the large probability transitions to the Γ_2 and $\Gamma_6^{(3)}$ states to occur. Table I shows the eigenfunctions of each CEF state. It is worth noting that the CEF splitting is reversed with respect to that generally given when the second-order term is preponderant. For instance, the states with mainly $|\pm7\rangle$ and $|0\rangle$ characters are the ground and first excited states, respectively, whereas the state ($\Gamma_5^{(1)}$) which mainly involves the $|\pm8\rangle$ eigenfunctions lies at a much larger energy. Taking into account the negative sign of B_2^0 one would expect a $|\pm8\rangle$ eigenfunction for the ground state and a $|0\rangle$ eigenfunction for the highest-energy state. This is due to the relative weakness of B_2^0 (-0.272 K) and consequently to a much larger effect of the other CEF pa-

TABLE II. Main characteristics and parameters of HoAlGa.

Parameters	Value (K)
B_2^0	-0.272
B_4^0	-6.83×10^{-4}
B_6^0	4.34×10^{-5}
B_6^6	1.47×10^{-4}
θ^*	-11.25
$J(0)$	-0.47
$J(Q)$	0.80
T_t	18.5
T_N	31

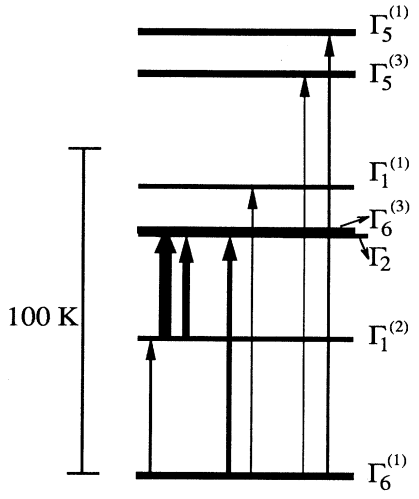

FIG. 5. Overall CEF level splitting of HoAlGa. Arrows indicate the main transitions observed by neutron spectroscopy. Arrow width is proportional to the transition probability.

rameters. This relative weakness of B_2^0 is consistent with that observed in the related $HoGa_2$ compound[15] where it is small and positive ($B_2^0 \approx 0.14$ K). It is likely to be associated with the various contributions arising from localized charges as well as conduction electrons.

IV. METAMAGNETIC PROCESSES AND THERMODYNAMIC PROPERTIES

A. The PF model

As described in the previous section, from a careful joint analysis of several experiments performed in the paramagnetic phase, we have been able to determine the four CEF parameters and the paramagnetic bilinear exchange coefficient $J(0)$ of HoAlGa. We have shown that, in this system, the ground state in the absence of a molecular field is a magnetic doublet, the first excited state is a nonmagnetic singlet, and the second and third excited states are a singlet and a doublet.

As quoted in the Introduction, a self-consistent periodic-field model has been recently developed to calculate the specific-heat anomaly at T_N in incommensurate amplitude modulated (AM) structures and subsequently extended to the description of the magnetization processes of such structures. We present hereunder the main characteristics of this model which has been previously described in more detail.[7,16] This PF model is based on an N-site Hamiltonian, N being the number of magnetic ions over one period of the AM magnetic structure. It is built from the single-site Hamiltonian valid in the paramagnetic phase (Sec. III):

$$\mathcal{H}=\sum_{i=1}^{N}\mathcal{H}_{\mathrm{CEF}}(i)+\sum_{i=1}^{N}\mathcal{H}_Z(i)+\sum_{i=1}^{N}\mathcal{H}_B(i)+\frac{1}{2}\sum_{i=1}^{N}\langle\mathbf{M}(i)\rangle\mathbf{H}_{\mathrm{ex}}(i)\ . \tag{8}$$

In this expression, the first two terms remain unchanged compared to Eqs. (2) and (3). Only the third and fourth terms, which are the bilinear exchange Hamiltonian and its associated corrective energy term due to the mean-field treatment, are different since they must include information about the magnetic modulation.

Due to the periodicity (propagation vector $\mathbf{Q}$), the magnetic moment $\mathbf{M}(j)$ as well as the exchange field

$$\mathbf{H}_{\mathrm{ex}}(i)=(g_J\mu_B)^{-2}\sum_{j\neq i}J(ij)\mathbf{M}(j)$$

can be expanded in a Fourier series:

$$\mathbf{M}(j)=\sum_n \mathbf{M}_{n\mathbf{Q}}e^{in\mathbf{Q}\mathbf{R}_j} \tag{9}$$

and

$$\mathbf{H}_{\mathrm{ex}}(i)=(g_J\mu_B)^{-2}\sum_n J(n\mathbf{Q})\mathbf{M}_{n\mathbf{Q}}e^{in\mathbf{Q}\mathbf{R}_i}\ , \tag{10}$$

where $J(\mathbf{q})$ is the Fourier transform of the exchange interaction $J(ij)$. It must be noticed that from the whole $J(\mathbf{q})$ variation, two parameters can be easily deduced from experiment, namely, $J(0)$ (see Sec. III) and $J(\mathbf{Q})$ which should account for the magnetic ordering at T_N. This latter is given by

$$J(\mathbf{Q})=\frac{(g_J\mu_B)^2}{\chi_0(T_N)}\ , \tag{11}$$

where χ_0 is the susceptibility without interaction which can be easily calculated as soon as the CEF parameters are known. The determination of the other coefficients $J(n\mathbf{Q})$ $(n\neq 1)$ would require the analysis of the magnetic excitations measured by inelastic neutron scattering in order to obtain $J(\mathbf{q})$ over the whole Brillouin zone.

From the self-consistent diagonalization of the Hamiltonian, Eq. (8), for the N ions over one magnetic period, one can calculate (i) the magnetic moment of each ion at any temperature and under any external magnetic field, (ii) the specific heat at any temperature.

Note that one of the most remarkable results obtained by this model concerns the specific-heat discontinuity at T_N which, in the case of an amplitude modulated structure, is given by

$$\Delta C_{\mathrm{AM}}=-\frac{1}{2}T_N\frac{[\chi_0'(T_N)]^2}{\chi_0^{(3)}(T_N)}=\frac{2}{3}\Delta C_{\mathrm{EM}}\ ,$$

where ΔC_{EM} is the discontinuity for an equal moment structure, and $\chi_0^{(3)}$ is the third-order susceptibility without interaction which, as for χ_0, can be calculated as soon as the CEF parameters are known.

B. Application to HoAlGa

As presented in Refs. 8 and 9, the magnetic structure of HoAlGa can be described by a single propagation vector $\mathbf{Q}_1=(\frac{1}{3},\frac{1}{3},\frac{1}{2})$ and its harmonics in phase I and a propagation vector $\mathbf{Q}_2=(\frac{1}{3},\frac{1}{3},0.481)$ in phase II (see Fig. 1). As $\mathbf{Q}_1$ and $\mathbf{Q}_2$ are very close, to simplify the problem we have used the commensurate $\mathbf{Q}_1$ vector in phase I as well

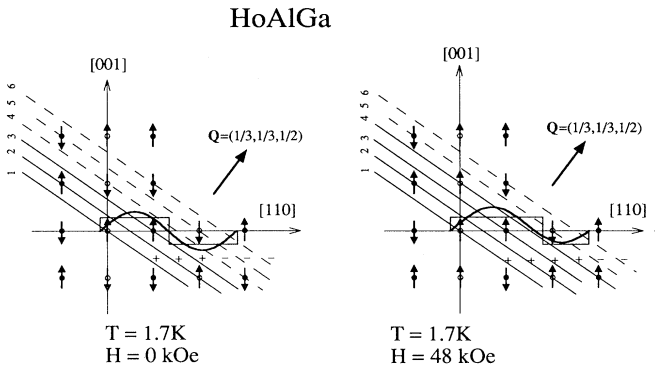

FIG. 6. Projections, on a plane perpendicular to the [1-10] direction, of the magnetic structure of HoAlGa at low temperature and in phases I and II. Solid and open circles represent atoms of the (1-10) plane passing through the origin and those of the parallel plane passing in the 1,0,0 position, respectively. The stacking of ferromagnetic planes perpendicular to the propagation vector $\mathbf{Q}_1$ is clearly disclosed. The squaring functions are the envelopes of magnetic moments. The sine wave modulations represent the variation of the exchange field when only $J(\mathbf{Q})$ and $J(0)$ are considered.

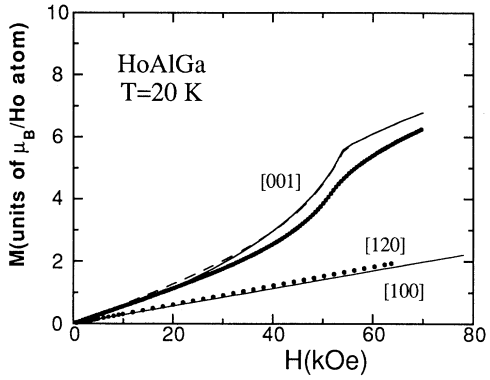

FIG. 7. Magnetization processes in HoAlGa at 20 K along the [001], [120], and [100] axes. Lines are calculations with the PF model using the commensurate $\mathbf{Q}_1$ propagation vector, i.e., taking into account six atoms over one period. The dashed line corresponds to the calculation with the true $\mathbf{Q}_2$ vector, i.e., taking into account 75 atoms over one period. (Although [120] is slightly easier than [100] their difference is too small to be visible on the experimental as well as calculated variations of the figure.)

as in phase II. Apart from phase III, all atoms in each plane perpendicular to the propagation vector $\mathbf{Q}_1$ form a ferromagnetic arrangement (Fig. 6). Six ferromagnetic planes have to be considered over one period. The sequence of planes are $++{+}{-}{-}{-}$ and $++{+}{-}{-}$ in phases I and II, respectively. When temperature is increased, the squaring progressively transforms into a sine wave modulation. So now the problem can be reduced to that of a linear chain of $N=6$ atoms over one period. If in phase II the true value of $\mathbf{Q}_2$ is used, about 75 atoms have to be considered over one period leading to much more complex calculations. However, from some selected tests we have found that this does not significantly change the calculated magnetization curves in the considered temperature range.

As shown in Fig. 6, if only $J(\mathbf{Q})$ and $J(0)$ are considered, the exchange field has a sine wave variation [which is not the case for $M(i)$ due to the nature of the ground state]. Most of the calculations in the present study using the PF model were carried out within this assumption which only uses parameters determined experimentally in the paramagnetic state.

1. *Magnetization processes*

The PF model is used for the calculation of magnetization processes using only the four CEF parameters, the paramagnetic exchange coefficient $J(0)=-0.47$ K and $J(\mathbf{Q})=0.80$ K associated with the Néel temperature T_N. The magnetization curves calculated at $T=20$ K (phase II), along the [001], [120], and [100] directions are presented in Fig. 7. Solid lines correspond to calculations performed over six atoms whereas along [001] the dashed line is the calculation over 75 atoms. The difference between the dashed and solid lines is very small and seems to confirm that, as long as $\mathbf{M}$ is still sine wave modulated (typically $T > T_N/2$), the magnetic processes only weakly depend on the size of the linear chain. Note that the agreement with experimental results is quite good taking into account that no additional parameters have been used. A pronounced cusp at 50 kOe is obtained by calculation and also observed experimentally along [001] which corresponds to the vanishing of the moment modulation (Fig. 8). Along the difficult magnetization directions [120] and [100], the curves are linear and practically merged, the magnetization being very slightly larger along [120] than along [100]. During this magnetization process, the modulated structure is twisted, the field inducing a component which is also modulated but with a period twice as small as along the easy [001] direction.

The observed and calculated magnetization curves at 10 K along the easy [001] axis in increasing and decreasing field are shown in Fig. 9. The experimental variation has no hysteresis and is characterized by two transitions: a tiny one around 26 kOe corresponding to the transition from phase I to phase II and a large, sharp one at 56.4 kOe when the ferromagnetic state is reached. The calculation also gives two transitions. Apart from the very weak difference between $\mathbf{Q}_1$ and $\mathbf{Q}_2$, the intermediate state calculated with $\mathbf{Q}_1$ is the same as that determined experimentally. The main difference between experiment and calculation concerns calculated hysteresis loops. The lower part of Fig. 9 shows the calculated field dependence of the free energy of the three phases. The crossing between the three variations occurs at 28.5 and 58.0 kOe, i.e., very close to the experimental critical field values. The hysteresis arises from potential barriers which have to be overcome. Calculation shows that a transition

occurs when the total field (applied plus exchange) on moments involved in the transition process changes sign.

The magnetization curve calculated with $\mathbf{Q}_2$, i.e., 75 atoms over one period, no longer exhibits a transition between phase I and II (dashed line in Fig. 9). The difference between this curve and the one calculated with $\mathbf{Q}_1$ allows us to understand the lack of experimental hysteresis. With $\mathbf{Q}_2$, over one period there is a much larger distribution of exchange field acting on the Ho moments. The transition from phase I to phase II does not arise from the magnetization reversal of exactly one over six planes for a given field but of approximately one over six planes distributed over a larger range of applied fields.

Above 10 K, magnetization curves calculated with $\mathbf{Q}_1$ along [001] exhibit a well-pronounced transition toward the ferromagnetic state but the amplitude of the first transition rapidly decreases when temperature increases and vanishes around 15 K. This is not surprising as, due to the appearance of the modulation, the only difference arises from the very small periodicity difference. This explains why experimentally no anomaly can be detected from magnetization measurements at T_t by susceptibility and specific heat. Only neutron diffraction has allowed us to determine the transition temperature. To truly account for the transition between phases I and II for 15 $K < T < T_t$, the model should consider that $J(\mathbf{Q}_2)$ is slightly larger than $J(\mathbf{Q}_1)$ and taken into account additional interactions which are much smaller than the CEF and exchange ones such as magnetoelastic and quadrupolar interactions.

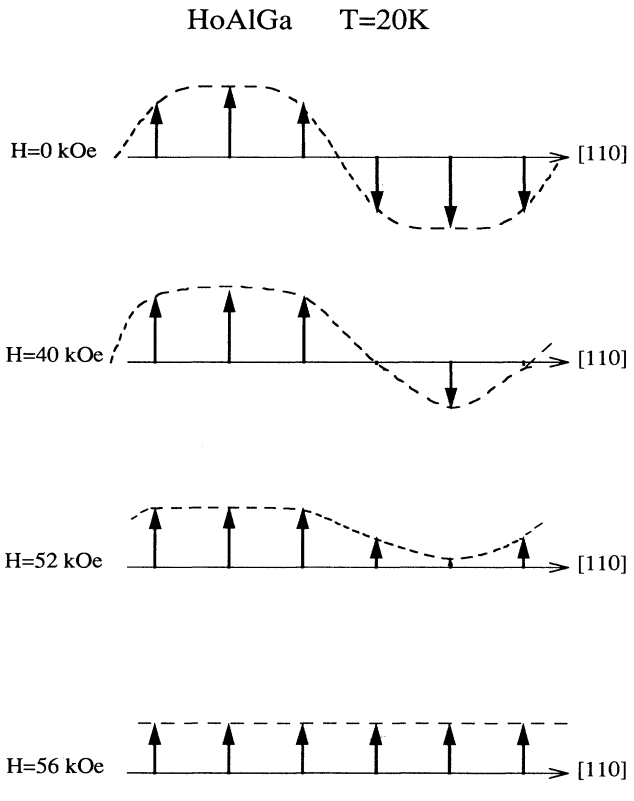

FIG. 8. Representation of the magnetic moments of HoAlGa, belonging to six successive planes perpendicular to the propagation vector $\mathbf{Q}_1$ under various fields at 20 K. This figure clearly shows that the cusp corresponds to the vanishing of the modulation.

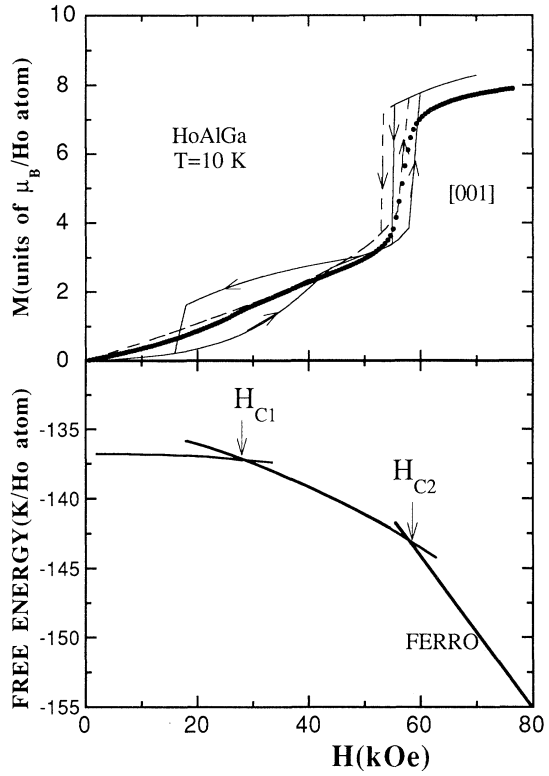

FIG. 9. Upper part: magnetization process at 10 K in HoAlGa in increasing and decreasing fields along the easy [001] direction. Solid circles, solid and dashed lines are experimental points and calculations performed with $\mathbf{Q}_1$ and $\mathbf{Q}_2$, respectively. Lower part: field dependences of the free energy at 10 K of phases I and II and in the ferromagnetic state calculated with $\mathbf{Q}_1$ along the same axis.

Below 6 K, phase III cannot be described as a stacking of ferromagnetic planes because it involves two propagation vectors,[9] namely, $(0,0,\frac{1}{3})$ and $(\frac{1}{3},\frac{1}{3},\frac{1}{3})$, in addition to $\mathbf{Q}_1$. The PF model then cannot predict this phase (simple Q calculation) and directly calculates the transition between phases I and II as above 6 K. The upper part of Fig. 10 shows experimental and calculated magnetization curves along [001] and [120] at 1.7 K in increasing and decreasing field. The lower part shows the calculated field dependences of the free energy of phases I, II, and of the ferromagnetic state (solid lines). As the Ho moment is practically field independent at this temperature, these energy variations are linear with slopes equal to 0, $-kM_0/3$, and $-kM_0$ for the three states, respectively, on account of their magnetic arrangements (k is a constant and M_0 is the Ho magnetic moment). The intersection of these lines defines the critical fields H_{c1} and H_{c2} which are the metamagnetic fields in the absence of hys-

teresis. H_{c1} and H_{c2} were calculated at different temperatures and their thermal dependences are reported as solid lines in Fig. 1. Therefore, from parameters determined only in the paramagnetic state and from the knowledge of the magnetic periodicities, the PF model gives a good account of the low-temperature magnetic phase diagram of HoAlGa.

On account of the magnetic arrangement of phase III,[9] the field dependence of the free energy at low temperature does have a linear variation with a slope three times smaller than in phase II as shown by the dashed line of Fig. 10. [The intersection with the energy axis cannot be determined because it depends on $J(n\mathbf{Q}_3)$, which are unknown.] One readily sees on this figure that the transition fields involved in phase III must be on both sides of H_{c1} in agreement with the experimental points reported in Fig. 1 as the boundary of this phase. Along the hard [120] direction, although slightly smaller, the calculated variation is in rather good agreement with the experimental one.

In the above calculation we have not considered the effect of higher-order $J(n\mathbf{Q})$ parameters with $n=2,3,\ldots$ because (i) they have very little effect as long as the magnetic structure is mainly sine wave modulated, i.e., near T_N, (ii) their determination needs the spin-wave dispersion obtained from inelastic neutron experiments on single crystals, (iii) the above calculations give a quite satisfactory analysis when they are neglected. However, it is worth evaluating their effect in particular on the hysteresis. Therefore, we have calculated magnetization curves for different values of $J(2\mathbf{Q})$ and $J(3\mathbf{Q})$. Along the hard axis their effect is negligible. Along the easy axis, they generally change both critical fields and hysteresis. An illustration of their role along the easy axis is given in Fig. 11 at 1.7 and 10 K for $J(2\mathbf{Q})=-0.21$ K and $J(3\mathbf{Q})=-0.42$ K. These values allow a decrease in the hysteresis without significantly changing the critical fields. Moreover, their order of magnitude is quite reasonable. However there remains a large hysteresis loop at 1.7 K for the highest transition. On the upper part of Fig. 11 is also reported the magnetization curve calculated at 10 K with the same values of $J(2\mathbf{Q})$ and $J(3\mathbf{Q})$ but

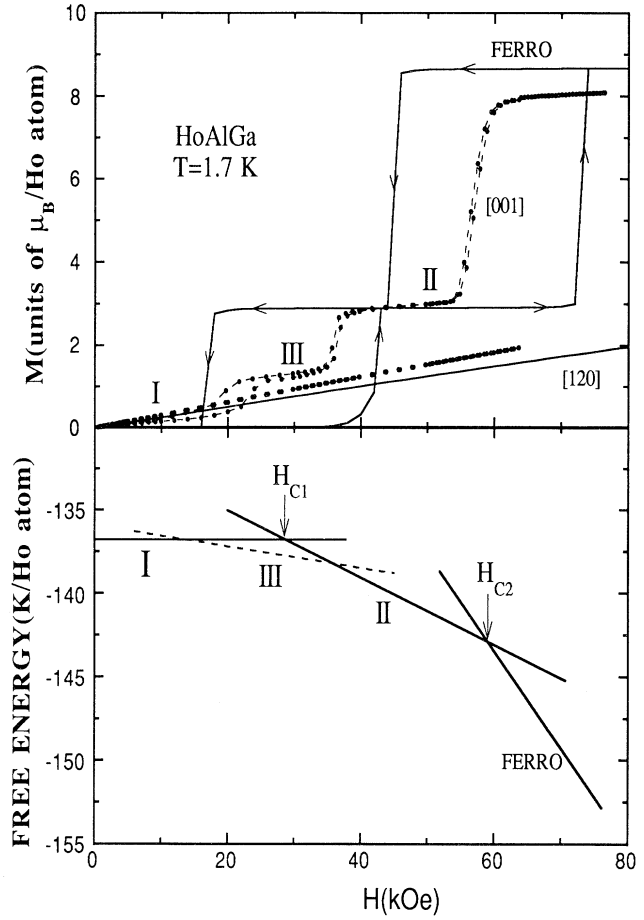

FIG. 10. HoAlGa, 1.7 K. Upper part: experimental and calculated magnetization process in increasing and decreasing fields along the [001] and [120] directions. Lower part: calculated field dependences along the [001] axis of the free energy at 1.7 K of phases I and II and in the ferromagnetic state (solid line). The dashed line is the energy variation of phase III. The crossing of this line with the energy axis cannot be calculated but its slope is well known on account of the fact that magnetization of this phase is $M_0/9$, where M_0 is the saturation magnetization.

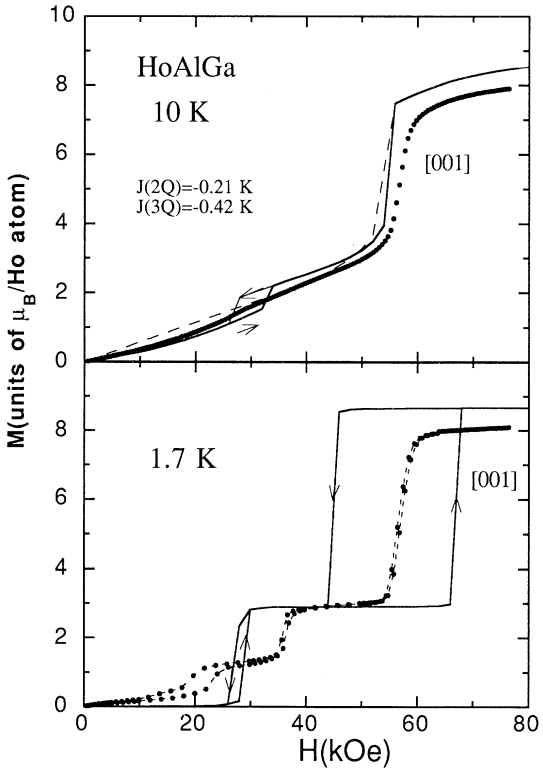

FIG. 11. Effect of $J(2Q)$ and $J(3Q)$ on the calculated magnetization curves along the [001] axis at 10 and 1.7 K (solid and dashed lines are the calculations performed with $\mathbf{Q}_1$ and $\mathbf{Q}_2$, respectively).

considering 75 atoms over one period ($\mathbf{Q}=\mathbf{Q}_2$). As for the previous calculation where these harmonics were not considered, there is no metamagnetic process corresponding to the transition between phases I and II.

From the different calculations one can make the following comments concerning the hysteresis of the metamagnetic processes.

(1) The experimental as well as calculated hysteresis increase when temperature is decreased due to thermal effects.

(2) The small value of the low-temperature experimental hysteresis compared to that calculated with $\mathbf{Q}_1$, i.e., a short period, is less due to (i) the crossing of an energy barrier through thermal fluctuations and/or (ii) the effect of higher $J(nQ)$ harmonics, than to the large distribution of exchange fields associated with the true incommensurate (or long-period commensurate) structure of phase II.

An interesting remark can also be made concerning the magnetization process calculated at 10 K with $\mathbf{Q}_1$ and $\mathbf{Q}_2$ (upper part of Fig. 11). At low field, i.e., in phase I, the true propagation vector is $\mathbf{Q}_1$ and the magnetization curve is better accounted for with this vector than with $\mathbf{Q}_2$. At larger field, i.e., in phase II, the magnetization curve is on the contrary better accounted for with $\mathbf{Q}_2$.

2. Susceptibility

The model has also been used for the analysis of the low-temperature initial susceptibility (Fig. 12). Without any additional parameter than $J(0)$, $J(\mathbf{Q})$, and the B_1^m's, calculation and experiment are in good agreement along [001] as well as along the hard [120] direction: a good order of magnitude, well-pronounced maximum at T_N along [001], almost no anomaly at this temperature along the hard axis. The model does not account for the observed plateau around 20 K. However, with the values of $J(2\mathbf{Q})$ and $J(3\mathbf{Q})$ used above, namely, -0.21 and -0.42 K, respectively, this feature is better accounted for. Along the hard axis, these extra parameters have a negligible effect.

3. Specific heat

The dashed line of Fig. 13 shows the thermal variation of the magnetic contribution to the specific heat calculated with the four CEF parameters and $J(\mathbf{Q})$. The general shape of the observed variation is well accounted for, keeping in mind that the experimental value strongly depends on the phonon contribution whose determination has a large uncertainty. In particular, a λ-type anomaly is predicted at T_N with a calculated discontinuity $\Delta C_{\mathrm{AM}} \sim 15.3$ J/K mol only slightly larger than the experimental value $\Delta C_{\mathrm{expt}} \sim 13.6$ J/K mol, while the jump expected for an equal moment system (dot-dashed line in Fig. 13) is noticeably larger, $\Delta C_{\mathrm{EM}} \sim 22.9$ J/K mol. Note that this ΔC_{expt} value has been estimated by taking into account a small contribution from magnetic fluctuations above T_N, as suggested by the comparison between theory and experiment in this temperature range. The calculation performed by also taking into account $J(3Q)=-0.42$ K (solid line in Fig. 13) does not significantly change the specific heat.

V. CONCLUSION

This paper shows that a model is able to give a quite satisfactory quantitative description of most of the magnetic and thermodynamic properties over a large temperature range (ordered and paramagnetic states) of antiferromagnetic compounds, even those with complex magnetic phase diagrams as is the case of HoAlGa. With a

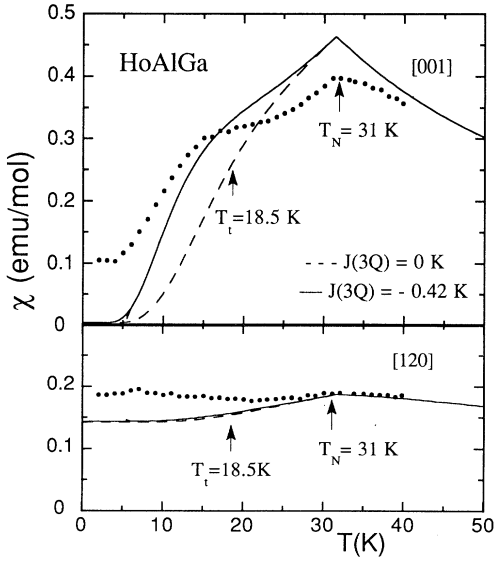

FIG. 12. Experimental and calculated [with $J(3Q)=0$ and -0.42 K] thermal dependences of the low-temperature magnetic susceptibility along the [001] (upper part) and [120] (lower part) directions.

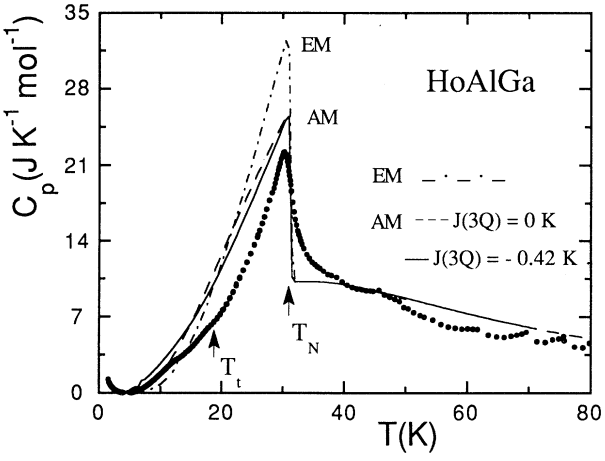

FIG. 13. Experimental and calculated thermal dependence of the specific heat of HoAlGa. The solid and dashed lines are the calculations considering the true magnetic structure which is, in particular amplitude modulated in a given temperature range below T_N. The dot-dashed line is the calculation considering that equal moment (EM) structure at any temperature below T_N.

limited number of parameters—namely, four CEF parameters, $J(0)$ and $J(\mathbf{Q})$ determined from inelastic neutron scattering, magnetization measurements in the paramagnetic state, and the value of T_N—the PF model has allowed us to calculate (i) the multistep magnetization processes (except phase III) with the correct values of the transition fields and the intermediate structures along the easy axis, (ii) magnetization curves along the hard axes, (iii) the amplitude and direction of each moment during all these processes, (iv) the thermal dependence of the initial susceptibility along and perpendicular to the easy axis, and (v) the specific heat with a good value of the discontinuity of the λ anomaly, and, in particular, its reduction in the case of amplitude modulated structures compared to that of equal moment structures. This model is valid as long as the different magnetic arrangements for different fields and temperatures can be described with a unique basis propagation vector $\mathbf{Q}$ [in addition to $\mathbf{Q}_0=(0,0,0)$ which obviously appears as soon as a magnetization is induced by the field] and/or vector multiple of $n\mathbf{Q}$ type. The problem is then reduced to that of a linear chain. The only failure of the model concerns the first field-induced magnetic structure below 6 K (phase III) which cannot be described as a stacking of ferromagnetic layers and therefore cannot be reduced to a linear chain. The extension of the PF model to the case of structures involving several noncolinear sublattices (multiple-$\mathbf{Q}$ structures) is in progress. This could allow the analysis of a still larger number of systems with complex magnetic phase diagrams.

ACKNOWLEDGMENTS

We are grateful to E. Bauer (T. U. Wien, Austria) and A. Murani (ILL, Grenoble) for their contribution in specific-heat and inelastic-neutron-scattering experiments, respectively.

[1]D. Gignoux and D. Schmitt, J. Magn. Magn. Mater. **100**, 99 (1991).

[2]J. Rossat-Mignod, P. Burlet, L. P. Regnault, and C. Vettier, J. Magn. Magn. Mater. **90&91**, 5 (1990).

[3]M. Date, J. Magn. Magn. Mater. **90&91**, 1 (1990).

[4]A. R. Ball, D. Gignoux, D. Schmitt, and F. Y. Zhang, J. Magn. Magn. Mat. **104–107**, 170 (1992), and references therein.

[5]J. A. Blanco, D. Gignoux, and D. Schmitt, Phys. Rev. B **43**, 13 145 (1991).

[6]J. A. Blanco, D. Gignoux, J. C. Gomez-Sal, and D. Schmitt, J. Magn. Magn. Mater. **104–107**, 1273 (1992).

[7]J. A. Blanco, D. Schmitt, and J. C. Gomez-Sal, J. Magn. Magn. Mater. **116**, 128 (1992).

[8]D. Gignoux, D. Schmitt, A. Takeuchi, F. Y. Zhang, C. Rouchon, and E. Roudaut, J. Magn. Magn. Mater. **98**, 333 (1991).

[9]A. R. Ball, D. Gignoux, D. Schmitt, F. Y. Zhang, and M. Reehuis, J. Magn. Magn. Mater. **110**, 343 (1992).

[10]A. P. Murani, Phys. Rev. B **28**, 2308 (1983); J. Phys. C **33**, 6359 (1983).

[11]A. R. Ball, D. Gignoux, and D. Schmitt, Physica B (to be published).

[12]M. T. Hutchings, Solid State Phys. **16**, 227 (1964).

[13]P. Morin and D. Schmitt, in *Ferromagnetic Materials*, edited by E. P. Wohlfarth and K. H. J. Buschow (North-Holland, Amsterdam, 1990), Vol. 5, Chap. 1.

[14]G. F. Korster, J. O. Dimmock, R. G. Wheeler, and H. Statz, *Properties of the Thirty-Two Point Groups* (MIT, Cambridge, 1963).

[15]D. Gignoux, D. Schmitt, and F. Y. Zhang (unpublished).

[16]J. A. Blanco, D. Gignoux, and D. Schmitt, Phys. Rev. B **43**, 13 145 (1991).